Article

Current Biology

Environmental representations in mouse hippocampal CA1 reflect the predictive structure of navigation

Graphical abstract

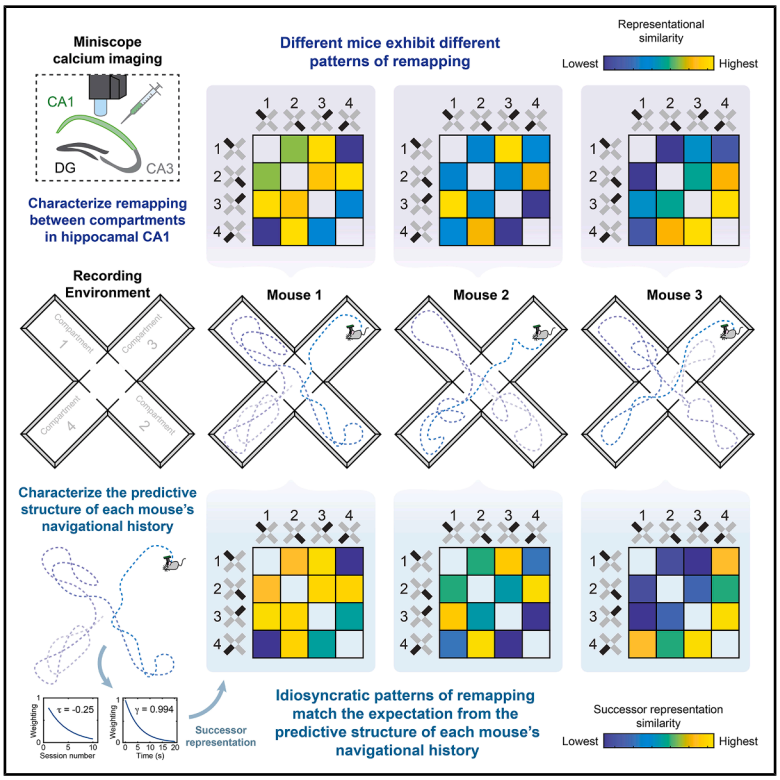

Highlights

- Different mice exhibited different patterns of remapping in a multicompartment space
- These coincided with differences in the predictive structure of their navigation
- Changing their navigational patterns induced corresponding representational changes
- A model encoding predictive structure on geometry-tuned inputs replicated results

Authors

Sergio A. Pecirno, Alexandra T. Keinath

Correspondence

atk@uic.edu

In brief

Recent theories propose that the structure of a navigator's cognitive map is determined by the predictive relationships they experience while navigating. Here, Pecirno and Keinath show that neural representations of space in the mouse hippocampus exhibit several hallmarks consistent with these predictive theories.

Pecirno & Keinath, 2025, Current Biology *35*, 1–14
December 15, 2025
https://doi.org/10.1016/j.cub.2025.11.010

CellPress

Current Biology

CellPress

Article

Environmental representations in mouse hippocampal CA1 reflect the predictive structure of navigation

Sergio A. Pecirno[1] and Alexandra T. Keinath[1,2,*]
[1]Department of Psychology, University of Chicago, Illinois, 1007 W Harrison Street, Chicago, IL 60607, USA
[2]Lead contact
*Correspondence: atk@uic.edu
https://doi.org/10.1016/j.cub.2025.11.010

SUMMARY

Predictive theories of cognitive mapping propose that these representations encode the predictive relationships among contents as experienced by the navigator. One hallmark of these theories is that representational structure in complex environments can be predicted from the behavioral history of the navigator. Here, we image neural activity in hippocampal CA1 as initially naive mice repeatedly navigate a multicompartment environment to test whether representational structure in this subregion is consistent with these predictions. We find that different mice instantiate different patterns of remapping across identically shaped compartments. Within a mouse, compartments with more similar predictive navigational histories on a particular spatiotemporal scale are represented more similarly, accounting for these individual differences. Manipulating navigational options induces reorganization of the CA1 structure, which specifically resembles the new predictive navigational structure on this timescale. Through computational modeling, we show that a combination of predictive encoding and geometrically structured inputs can uniquely account for this pattern of results. Together, these results demonstrate that the predictive structure of navigation is one important determinant of CA1 representations in complex environments, consistent with predictive theories of cognitive mapping.

INTRODUCTION

In order to survive and thrive, organisms—from mice to humans—rely on mnemonic representations of the external world and their relationships to it.[1] Referred to as "cognitive maps," these representations are instantiated by the coordinated activity of spatially tuned neural populations in the hippocampus and neighboring cortices.[2,3] Cognitive maps are often thought to represent the layout of the world,[4,5] motivated in part by the plethora of cells tuned to geometric features—locations, distances, and angles—found throughout the hippocampal formation and neighboring cortices.[2,6–20] Yet recent theories instead posit that cognitive maps represent the predictive relationships among their contents as experienced by the navigator,[21–24] with geometrically structured inputs (among others) providing a scaffold upon which predictive structure can be learned.[3,25–27]

Because the layout of an environment often determines the predictive relationships that the navigator experiences, and because modifying navigation often entails modifying the layout of the world, it can be difficult to disentangle the contributions of the two. Nevertheless, there are fundamental differences between predictive and world-centered theories. One hallmark of predictive theories is that the way in which a navigator explores a space is a critical determinant of the structure of their cognitive map.[21] If navigators explore the same space differently, then their cognitive maps should be structured differently, in a way which can be predicted from their navigational patterns. These differences should manifest across levels of explanation, from neural instantiations through behavior, and from the activity of single cells through the representational geometry of neural populations.

Motivated in part by these predictions, a growing body of work is characterizing the behavioral determinants of neural activity in the hippocampus and functionally related cortices.[8,15,28–36] In many cases, this work has demonstrated behavioral modulation of activity at the level of single cells and moment-to-moment population trajectories, which can be consistent with predictive theories.[15,31,32,35–37] Beyond these, predictive theories also make concrete claims about how behavior should determine the representational similarity among locations in complex environments consisting of multiple subspaces.[21] Within the hippocampus, representational similarity is reflected in the degree of decorrelation in the population response within or between spaces, known as "remapping." Prior work has demonstrated that remapping depends on the features shared between spaces,[38–42] past experience with those spaces,[39,43–46] and the broader reference frames in which those spaces are situated.[44] Individual differences in the degree of remapping within the same paradigm have been observed,[47] suggesting that remapping is not determined by world features and prior experience alone and can vary between navigators. Each of these characteristics might be understood within a predictive framework as resulting from changes to input features and/or the experience-dependent encoding of predictive structure.

Please cite this article in press as: Pecirno and Keinath, Environmental representations in mouse hippocampal CA1 reflect the predictive structure of navigation, Current Biology (2025), https://doi.org/10.1016/j.cub.2025.11.010

Yet predictive theories make even more specific predictions about patterns of hippocampal remapping in complex spaces.[21] So far, empirical tests have not conformed to these predictions,[48] calling into question whether the structure of hippocampal representations in these spaces can be understood through this lens. Notably, this previous test included multiple complexities—such as extensive prior experience in the environment as well as short-term changes to navigational options and the reward landscape—which make deriving concrete predictions from a predictive framework more challenging. Here, we test whether patterns of hippocampal remapping in complex spaces conform to a predictive framework in a simpler paradigm that avoids some of these complexities. Specifically, we characterize population activity in hippocampal CA1 as initially naive mice repeatedly explore four identically shaped, connected compartments in the absence of reward. To do so with high fidelity and across long timescales, we rely on chronic miniscope imaging. We test three hypotheses. If CA1 representational structure conforms to a predictive framework, then (1) mice that navigate differently should exhibit different patterns of remapping across compartments; (2) within a mouse, compartments with more similar predictive navigational histories should be represented more similarly; and (3) changing the navigational trajectory of a mouse should change its representational structure to better resemble the new predictive structure. Evidence against any of these hypotheses would support an alternative theory.

In all cases, our data support the predictive claims. That is, we find that different mice exhibit different patterns of remapping across compartments. These patterns coincide with the similarity of predictive navigational histories on a seconds-long timescale, modestly overweighting early experience. Manipulating the navigational trajectory of the mouse induces a reorganization of the CA1 representational structure, which specifically resembles the new predictive structure on this timescale, with a reversion to the previous pattern when relaxed. Leveraging computational modeling, we show that key results can be accounted for by a combination of predictive encoding operating on geometrically structured inputs; neither predictive encoding nor geometrically structured inputs were on their own sufficient to reproduce our pattern of results. Together, these results demonstrate that the behavioral history of the navigator is one important determinant of hippocampal representations in complex environments, consistent with predictive theories of cognitive mapping.

RESULTS

Characterizing CA1 representational structure in a multicompartment environment

We recorded daily from hippocampal CA1 via miniscope calcium imaging (Figure 1A) as initially naive mice (n = 11; 6 male) navigated a radial multicompartment environment. This environment consisted of four 20 × 35 cm rectangular compartments connected by a central chamber (Figure 1B). Each session lasted either 30 or 40 min, depending on imaging signal strength, to maximize the amount of data while minimizing the impact of photobleaching. Both miniscope and behavioral data were simultaneously recorded at a sampling rate of 30 Hz, and behavioral data were linearly interpolated for each imaging frame on the basis of system clock timestamps. In the first phase of the experiment, initially naive mice navigated this environment freely for between five and fifteen sessions (n = 121 sessions total). We refer to these sessions as free$_1$. The environment was not baited with rewards during any phase of the experiment.

For each session, imaging data were first motion corrected.[49] Next, cells were segmented, and their calcium traces were extracted via constrained nonnegative matrix factorization (CNMFE; Figure 1A).[50,51] For each trace, the likelihood of spiking events giving rise to that trace were inferred through a second-order autoregressive deconvolution algorithm[52] (Figure 1A). This nonnegative vector was then binarized such that any frame with a nonzero likelihood was treated as active (i.e., 1), otherwise it was treated as not active (i.e., 0). All further analysis was conducted on this binary activity vector.

To characterize the extent to which spatial location modulated the activity of each cell, we computed a rate map for each cell summarizing the mean activity of that cell as a function of location within the environment (Figure 1C). Next, we computed the split-half stability and spatial information content of this rate map. To assess the significance of these measures, we compared these values with surrogate distributions computed by circularly shifting the activity vector relative to the position vector 1,000 times. Cells with split-half stability and spatial information content exceeding the 95th percentiles of both distributions were considered spatially tuned and included in further analysis, though relaxing these criteria did not qualitatively change our results. Generally, the majority of cells met these criteria (Figure 1D), with lower proportions of cells meeting criteria in mice with shorter recording durations and qualitatively weaker signal.

Prior work in multicompartment environments has demonstrated that individual CA1 cells tend to be active in multiple compartments,[53,54] making comparisons between compartments meaningful. We confirmed that this was the case in our data. To do so, for each cell, we computed its mean activity rate in each compartment and sorted these from the most-active to the least-active compartments. Across sessions, we found that mean activity rates remained high in all compartments, with, on average, at least ~1 active frame per second even in dispreferred compartments (Figure 1E). The difference in activity rate between preferred and dispreferred compartments was approximately 3-fold. Interestingly, we also observed changes in mean activity rates with experience in dispreferred (but not preferred) compartments (Figure 1F). Reflecting this, a linear mixed effects model of changes in mean activity rates as a function of compartment and session number, with mouse ID as a random factor, revealed a significant interaction between compartment and session ($F(3,396) = 3.84$, $p = 0.0099$). Neither main effects of compartment nor session number reached significance ($F(3,396) = 0.81$, $p = 0.4947$ and $F(1,396) = 0.21$, $p = 0.6515$, respectively). These results are consistent with the development of sparsity and/or sharpening of the spatial code across experience.[55]

Different mice instantiate distinct and persistent patterns of remapping across identical compartments

Predictive theories claim that CA1 representational structure should be determined, at least in part, by the predictive structure

Please cite this article in press as: Pecirno and Keinath, Environmental representations in mouse hippocampal CA1 reflect the predictive structure of navigation, Current Biology (2025), https://doi.org/10.1016/j.cub.2025.11.010

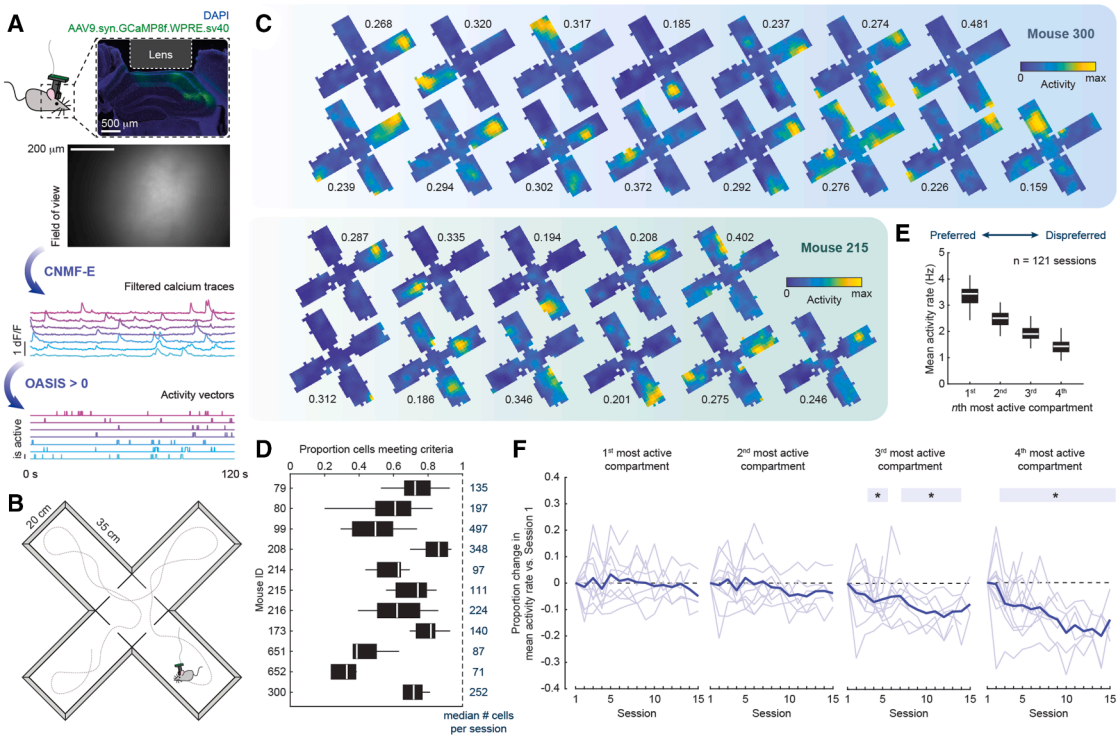

Figure 1. Characterizing mouse CA1 in a multicompartment environment via miniscope imaging

(A) Schematic of miniscope imaging and data-processing pipeline.

(B) Schematic of the multicompartment environment.

(C) Example rate maps from simultaneously recorded cells for one session from two mice. Peak activity rate in proportion of active frames noted for each map.

(D) Proportion of cells with split-half stability and spatial information content exceeding the 95th percentile of their shuffled controls across sessions for each mouse. Median number of cells per session for each mouse noted on the right.

(E) Mean activity rate as a function of most-active to least-active compartments.

(F) Change in mean event rate versus the first session, as a function of most-active to least-active compartments. Soft lines are individual mice. Bold line is the mean across mice. Shaded box denotes sessions for which $p < 0.05$. Significance markers denote the outcome of an uncorrected t test versus zero for a given compartment and session. *$p < 0.05$.

of one's navigational trajectory. If so, then we would expect mice in our paradigm to instantiate different patterns of remapping between compartments insofar as they navigate with different trajectories. Although individual differences in representational structure might also be expected on many other bases, evidence against such individual differences would challenge the predictive claim. On the other hand, if the layout of the environment alone determines representational structure, then we might expect mice in our paradigm to instantiate similar patterns of remapping. Such common structure might correspond to key geometric features, such as the distance between compartments or the relative orientations of the compartments.[53,54]

To address these possibilities, we characterized the degree of remapping between compartments in our data using a population vector (PV) approach. To this end, for each cell, we first computed a separate rate map for each compartment (Figure 2A). Next, for each session, we computed the PV correlations between all pairwise comparisons of compartment rate maps, aligned by their entryways and excluding unsampled pixels (Figure 2A). PV correlations summarize the degree to which two spaces are represented similarly at the level of the neural population in a way that captures changes in both firing rates and spatial tuning. Computing all pairwise PV correlations between compartments yields a 4 × 4 matrix, which we refer to as the "PV structure" (Figure 2A). Finally, we correlated PV structures between sessions and compared correlations between different sessions from the same mice to correlations between sessions from different mice (Figure 2B).

Consistent with the predictive theory, comparisons of sessions from the same mouse resulted in significantly higher correlations than comparisons between mice (Figures 2C and 2D). Moreover, despite the limited number of comparisons defining the PV structure (i.e., six pairwise comparisons between the four compartments), these differences were so reliable that a simple Euclidean distance-based classifier could correctly predict mouse identity well above chance (accuracy = 45.45%, chance = 9.09%, p = ~0; binomial test). This reliable structure was present even though PV correlation values between compartments were generally low in magnitude (Figure 2E), suggesting that even weak correlations in representational structure can be stable and informative.[56] Even averaging within a mouse, PV structures varied widely between mice and qualitatively did not come to resemble a consistent geometric feature of the compartmental layout (i.e., distance, entryway angle, long axis, etc.; Figure 2F). Similar results were observed when correlating mean activity rates as the measure of remapping (Figure S1),

Please cite this article in press as: Pecirno and Keinath, Environmental representations in mouse hippocampal CA1 reflect the predictive structure of navigation, Current Biology (2025), https://doi.org/10.1016/j.cub.2025.11.010

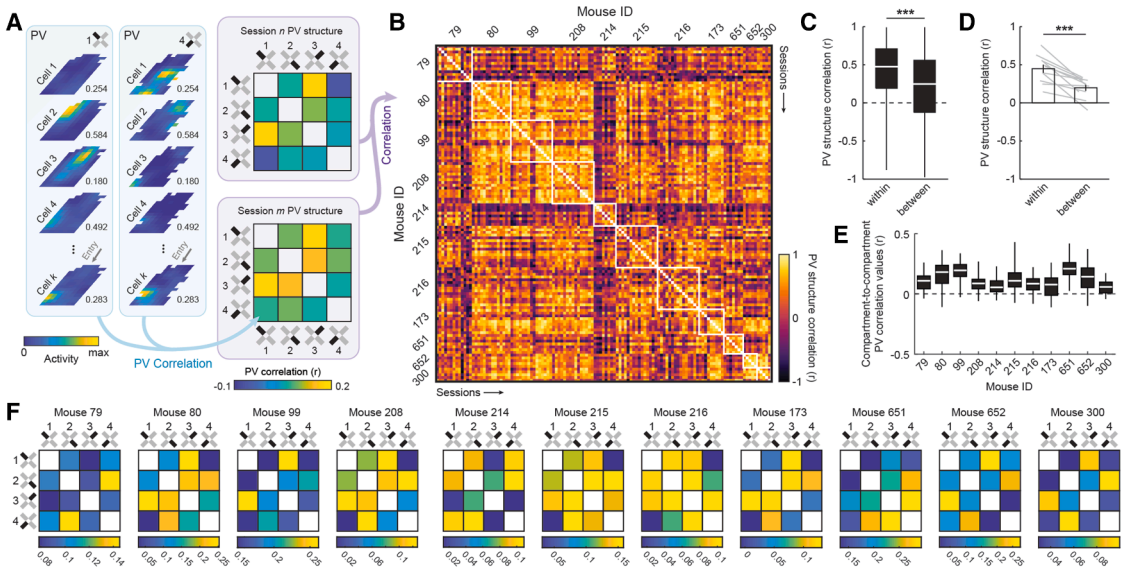

Figure 2. Individual differences in patterns of remapping across compartments in a multicompartment environment

(A) Schematic of PV structure analysis pipeline. Rate maps scaled to peak activity rate across all compartments. This peak rate is noted next to each map.

(B) PV structure correlations across all pairwise comparisons of sessions. White boxes bound session comparisons from the same mice.

(C) PV structure correlations for comparisons within a mouse versus between different mice, treating each pairwise session comparison independently (rank-sum test: $Z(3143353) = 11.879$, $p = 1.513e{-}32$).

(D) PV structure correlations for comparisons within a mouse versus between mice, treating each mouse as the unit of analysis (signed-rank test: $p = 9.766e{-}04$). Soft lines denote individual mice. Error bars denote SEM across mice.

(E) Distribution of compartment-to-compartment PV correlation values for each mouse.

(F) PV structures averaged across sessions for each mouse.

See also Figures S1, S2, and S3. ***$p < 0.001$.

indicating that our results are not dependent upon the rate-map-based assumptions underlying PV correlations. Mice also varied in the extent to which competing reference frames oriented repeating place fields across compartments (Figure S2). Together, these results demonstrate that mice instantiate idiosyncratic patterns of remapping across compartments in this multicompartment paradigm.

Idiosyncratic CA1 representational structure matches the predictive structure of navigation on a particular spatiotemporal scale

Our previous results demonstrate reliable individual differences in CA1 representational structure in mice navigating our multicompartment environment. Although these differences could arise from predictive cognitive mapping, individual differences are not on their own unique to this theory. For example, a geometric theory might predict individual differences if navigators are attending to or naturally emphasize different features of the world. Therefore, we next tested the more specific claim of predictive theories: that individual differences in CA1 representational structure arise due to idiosyncratic navigational differences. If correct, then compartments with more similar predictive navigational structures should be represented more similarly in CA1.

To test this possibility, we leveraged one formalization of predictive cognitive mapping, the successor representation.[21] At a high level, the successor representation defines the behavioral determinants of hippocampal representational structure as the temporally discounted probabilities of transitioning between locations within an environment. This is expressed as a successor matrix M, such that

$$M = \sum_{t=0}^{\infty} \gamma^t T^t = (I - \gamma T)^{-1}, \qquad \text{(Equation 1)}$$

where T^n is the n-step transition matrix capturing the probability of transitioning from one location to another after n timesteps, γ is the temporal discount factor that determines how heavily transitions near in time versus far in time are discounted, and I is the identity matrix.

In our case, for a given session s, we can compute the successor matrix $M_{s,k}$ separately for each compartment k. Correlating these matrices between all pairwise comparisons of compartments yields a 4×4 matrix, which we can compare to the PV structure for that session. If the predictive claim is correct, then these matrices should be correlated. Importantly, though, in our paradigm, mice explored the environment for multiple sessions, and it is not obvious whether navigation during every session should have an equal impact on CA1 representational structure. Although this is certainly a possibility, it is also possible that more recent behavior or early behavior has an exaggerated impact on determining CA1 representational structure. The longitudinal nature of our recording paradigm allows us to test these possibilities. To do so, for each session s and compartment k, we computed a cumulative one-step transition matrix $C_{s,k}$ from all navigational data, up to and including that session, such that

Please cite this article in press as: Pecirno and Keinath, Environmental representations in mouse hippocampal CA1 reflect the predictive structure of navigation, Current Biology (2025), https://doi.org/10.1016/j.cub.2025.11.010

CellPress

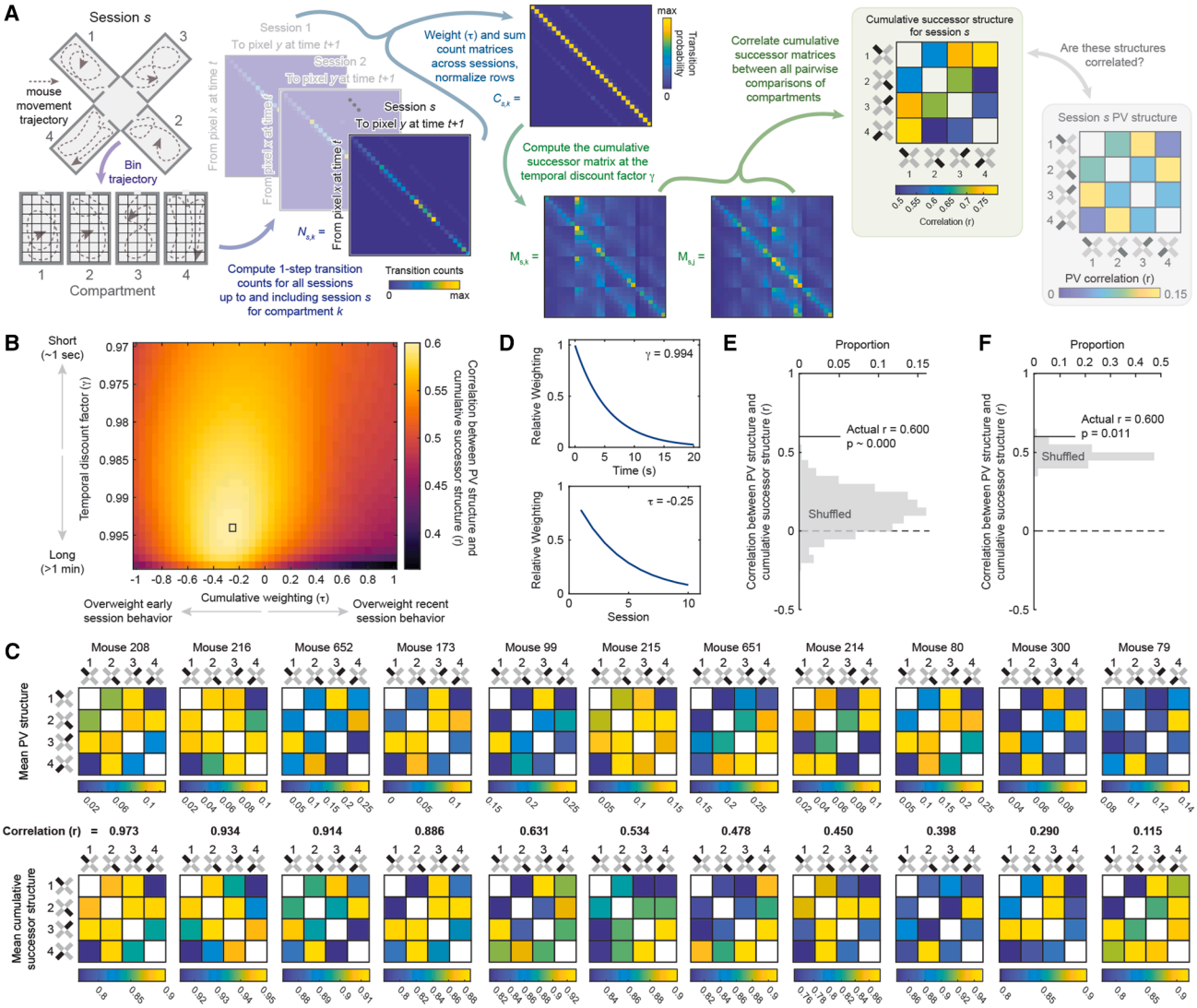

Figure 3. CA1 PV structure matches the similarity of predictive navigational structure on a particular spatiotemporal scale

(A) Schematic of pipeline for computing cumulative successor structure.

(B) Grid search where γ and τ are varied and the mean cumulative successor structure is correlated with the mean PV structure for each mouse.

(C) Mean PV structures and mean cumulative successor structures for all mice, with correlations noted. Ordered from most to least correlated.

(D) Relative weightings derived from γ and τ at maximizing parameterizations.

(E) Correlation between PV structure and cumulative successor structure against a shuffled control where transition count matrices are shuffled across compartments, mice, and sessions and controlling for the grid search.

(F) Correlation between PV structure and cumulative successor structure, against a shuffled control, where transition count matrices are shuffled across sessions within a mouse and the grid search is controlled for.

See also Figure S3.

$$C_{s,k} = \left[\sum_{i=1}^{s} e^{(\tau i)} N_{i,k}\right]_{\oslash}, \qquad \text{(Equation 2)}$$

where $N_{i,k}$ is the one-timestep transition count matrix for session i and compartment k, τ determines the exponential weight with which each session's transition counts contribute to the cumulative transition matrix, Σ denotes element-wise summation across sessions, and $\oslash$ denotes row normalization, such that each element is divided by the sum of all elements in its row (Figure 3A). A negative value of τ will overweight early session behavior. A positive value of τ will overweight more recent behavior. A τ of zero will equally weight behavior from all sessions. Substituting $C_{s,k}$ for T in Equation 1, we can compute the cumulative successor matrix $M_{s,k}$ for each session s and compartment k, such that

$$M_{s,k} = \left(I - \gamma C_{s,k}\right)^{-1}. \qquad \text{(Equation 3)}$$

Finally, we can correlate $M_{s,k}$ between all pairwise comparisons of compartments (excluding unsampled pixels), yielding the 4×4 matrix, which we refer to as the "cumulative successor

Please cite this article in press as: Pecirno and Keinath, Environmental representations in mouse hippocampal CA1 reflect the predictive structure of navigation, Current Biology (2025), https://doi.org/10.1016/j.cub.2025.11.010

structure" (Figure 3A). This matrix summarizes the similarity in predictive navigational structure between compartments, dependent upon two parameters, γ and τ. These parameters determine the time horizon of the encoded predictive structure and the weighting of cumulative experience, respectively.

To determine whether cumulative successor structures match CA1 PV structures at any parameterization, we conducted a grid search where γ and τ were varied and the mean successor structure was correlated with the mean PV structure for each mouse. This analysis revealed that mean successor structures were highly correlated with mean PV structures at a particular subset of parameterizations, with a maximum at $\gamma = 0.994$ and $\tau = -0.25$ (Figures 3B, 3C, and S3A). These parameters correspond to a seconds-long timescale for encoding predictive structure, modestly overweighting early experience (Figure 3D). To assess the significance of the high correlation that we observed at this parameterization (mean $r = 0.600$), we considered several controls. First, we compared this value to the distribution we might expect from generic mouse behavior by randomly shuffling transition count matrices (i.e., N in Equation 2) between compartments, sessions, and mice prior to computing cumulative successor structures. To account for the selection of the maximizing parameterization from our grid search, we repeated our grid search for each shuffle and took the maximum correlation for that shuffle. The true correlation exceeded this control (nonparametric $p \sim 0.000$, 1,000 shuffles; Figure 3E). Next, we tested whether the specific order of experience mattered by randomly shuffling transition count matrices across sessions separately for each mouse before computing cumulative successor structures and choosing the maximum correlation across the grid search for each shuffle. Again, the true correlation exceeded this control (nonparametric $p = 0.011$, 1,000 shuffles; Figure 3F). Repeating these analyses but treating individual sessions as the unit of analysis rather than individual mice yielded similar results (Figure S3). Substituting mean activity rates as the measure of remapping also yielded similar results (Figure S3), indicating that the concordance between predictive structure and degree of remapping we observe is not dependent upon the rate-map-based assumptions inherent in PV correlations. We note that positive values of τ, which overweight current session experience, yielded numerically weaker correlations between successor structures and PV structures. This provides additional evidence that the concordance we observe between these structures at maximizing parameterizations is not due to low-level within-session confounds. Together, these results demonstrate that compartments with more similar predictive navigational structures on a particular spatiotemporal scale are represented more similarly in CA1, consistent with a predictive theory of cognitive mapping.

To gain more insight into how predictive navigational structure varied within and between mice on this critical timescale ($\gamma = 0.994$), we next computed individual session (non-cumulative) successor structures and correlated these structures between sessions (Figure 4A). Successor structures were modestly more correlated within a mouse than between mice (Figures 4B and 4C), suggesting some consistency in behavioral patterns across sessions within a mouse. However, this varied considerably between mice, with some mice showing little to no consistency in successor structures across sessions. This variability is useful for distinguishing the relative weightings of cumulative behavior (i.e., τ), as consistent predictive structure across sessions makes it difficult to parse out the relative contributions of individual sessions. It also suggests that the greater degree of consistency we observe in the CA1 PV structure across sessions is not due to consistent behavior from session to session alone but rather reflects integration of experience across time.

Finally, we asked whether other behavioral determinants might explain CA1 PV structure equally well. We first tested whether transitions between compartments were equally correlated with PV structure, as might be expected from some instantiations of a predictive theory.[21,48] To this end, for each session, we computed the cumulative number of transitions between each pair of compartments across all sessions, up to and including that session (Figure 4D). As before, it is unclear whether experience during different sessions should be weighted equally. Thus, we weighted the contributions of each session as in Equation 2 and determined the maximizing τ through a grid search at the same resolution as before (i.e., Figure 3B). Even at maximizing τ, these matrices were significantly less correlated with PV structures than cumulative successor structures (Figure 4E).

Next, we asked whether differences in velocity, time spent in each compartment, thigmotaxis, or general sampling patterns could equally account for PV structure (Figure S4). Neither the similarity of velocity—measured as the inverse absolute difference between mean velocity in each compartment—nor higher mean velocities could account for PV structure as well as cumulative successor structure (Figures 4F and 4G). Neither the similarity of occupancy times—measured as the inverse absolute difference between total occupancy time in each compartment—nor longer mean occupancy times could account for PV structure as well as cumulative successor structure (Figures 4H and 4I). Neither similar degrees of thigmotaxis—measured as the inverse absolute difference between the proportion of time spent within 5 cm of a wall in each compartment—nor higher mean degrees of thigmotaxis could account for PV structure as well as cumulative successor structure (Figures 4J and 4K). Even the similarity of sampling patterns—measured as the correlation between pixel occupancy maps within each compartment—could not account for PV structure as well as the cumulative successor structure. This was true regardless of whether we compared only the sampling for a given session or the cumulative sampling for all sessions, up to and including that session (Figures 4L and 4M). Together, these results demonstrate that cumulative successor structures uniquely resemble CA1 representational structure, even when compared with other associated behavioral metrics.

Manipulating navigational options induces reorganization of CA1 representational structure to match the new predictive structure of navigation

Our previous results demonstrate that CA1 exhibits individual differences in the degree of remapping between compartments that coincide with the similarity of predictive structure on a particular spatiotemporal scale. Although these results provide correlational evidence consistent with a predictive theory of cognitive mapping, these theories make a stronger causal claim. That is, changing the movements of a navigator should induce a

Please cite this article in press as: Pecirno and Keinath, Environmental representations in mouse hippocampal CA1 reflect the predictive structure of navigation, Current Biology (2025), https://doi.org/10.1016/j.cub.2025.11.010

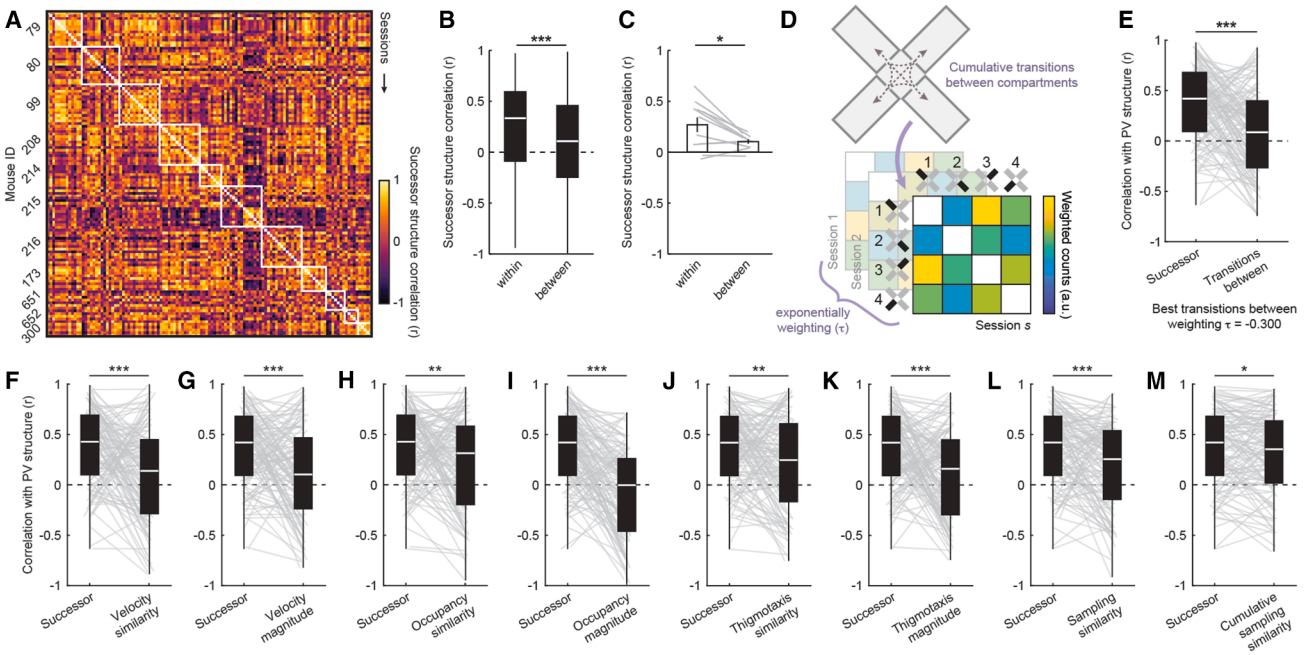

Figure 4. Successor structures are modestly stable across sessions, and cumulative successor structures better explain PV structure than other behavioral variables

(A) Noncumulative successor structure correlations across all pairwise comparisons of sessions. White boxes bound session comparisons from the same mice. Note that some mice exhibit high correlations across sessions, while others do not.

(B) Successor structure correlations for comparisons within a mouse versus between different mice, treating each pairwise session comparison independently (rank-sum test: $Z(2964100) = 8.466$, $p = 2.545e{-}17$).

(C) Successor structure correlations for comparisons within a mouse versus between different mice, treating each mouse as the unit of analysis (signed-rank test: $p = 3.223e{-}02$). Soft lines denote individual mice. Error bars denote SEM across mice.

(D) Schematic for computing cumulative weighted transitions between compartments.

(E) PV structures were more highly correlated with cumulative successor structures than cumulative transitions between compartments (signed-rank test: $Z(5609) = 4.962$, $p = 6.963e{-}07$). Sessions treated independently.

(F) As in (E), except for velocity similarity ($Z(5405) = 4.435$, $p = 9.219e{-}06$).

(G) As in (E), except for higher mean velocities ($Z(5253) = 4.042$, $p = 5.309e{-}05$).

(H) As in (E), except for the similarity of occupancy times ($Z(4769) = 2.790$, $p = 5.276e{-}03$).

(I) As in (E), except for higher mean occupancy times.

(J) As in (E), except for more similar degrees of thigmotaxis ($Z(4941) = 3.235$, $p = 1.218e{-}03$).

(K) As in (E), except for higher mean degrees of thigmotaxis ($Z(5285) = 4.124$, $p = 3.718e{-}05$).

(L) As in (E), except for the similarity of sampling distributions ($Z(5270) = 4.086$, $p = 4.397e{-}05$).

(M) As in (E), except for the similarity of cumulative sampling distributions ($Z(4528) = 2.166$, $p = 3.029e{-}02$). $^{*}p < 0.05$, $^{**}p < 0.01$, $^{***}p < 0.001$.

See also Figure S4.

corresponding change in representational structure to match the new predictive structure. We next sought to test this prediction. To this end, in four of our mice, we followed the initial free navigation phase (15 sessions; "Free$_1$") with an additional phase of limited navigation (7 sessions; "Limited") and, finally, a subsequent free navigation (21 sessions; "Free$_2$"; Figure S5). During the Limited phase, each session consisted of locking the mouse in each compartment for 4 min at a time, twice per session. Locking was achieved by the experimenter placing a small barrier in the entryway. This barrier was made of the same material as the walls and fit snuggly in the entryway, matching its dimensions. When each 4-min epoch ended, the door was removed and the mouse freely navigated in clockwise order to the next compartment.

Extensive evidence indicates that manipulating environmental features[39,40,44–46,57] and behavioral contingencies[58–60] can induce remapping in hippocampal CA1. We therefore reasoned that limiting navigational options, a novel experience for the mouse, would lead to remapping in CA1 during which new predictive structure might be encoded. Moreover, although this manipulation does not enforce a particular change to their navigational trajectories, free navigation typically involved shorter bouts of exploration within each compartment (median bout duration = 11.13 ± 4.92 s; mean ± standard deviation across Free$_1$ sessions). Thus, we suspected that limiting options would also lead mice to deviate from their free navigational patterns.

We first confirmed that our manipulation did indeed induce remapping in CA1. To do so, we correlated PV structures across all sessions within each mouse and compared correlations between different phases of this experiment. Limiting navigational options led to a clear reorganization of PV structure, on average and separately in each mouse (Figure 5A). Quantifying this, correlations between Free phases and the Limited phase were significantly lower than correlations within the same phase

Please cite this article in press as: Pecirno and Keinath, Environmental representations in mouse hippocampal CA1 reflect the predictive structure of navigation, Current Biology (2025), https://doi.org/10.1016/j.cub.2025.11.010

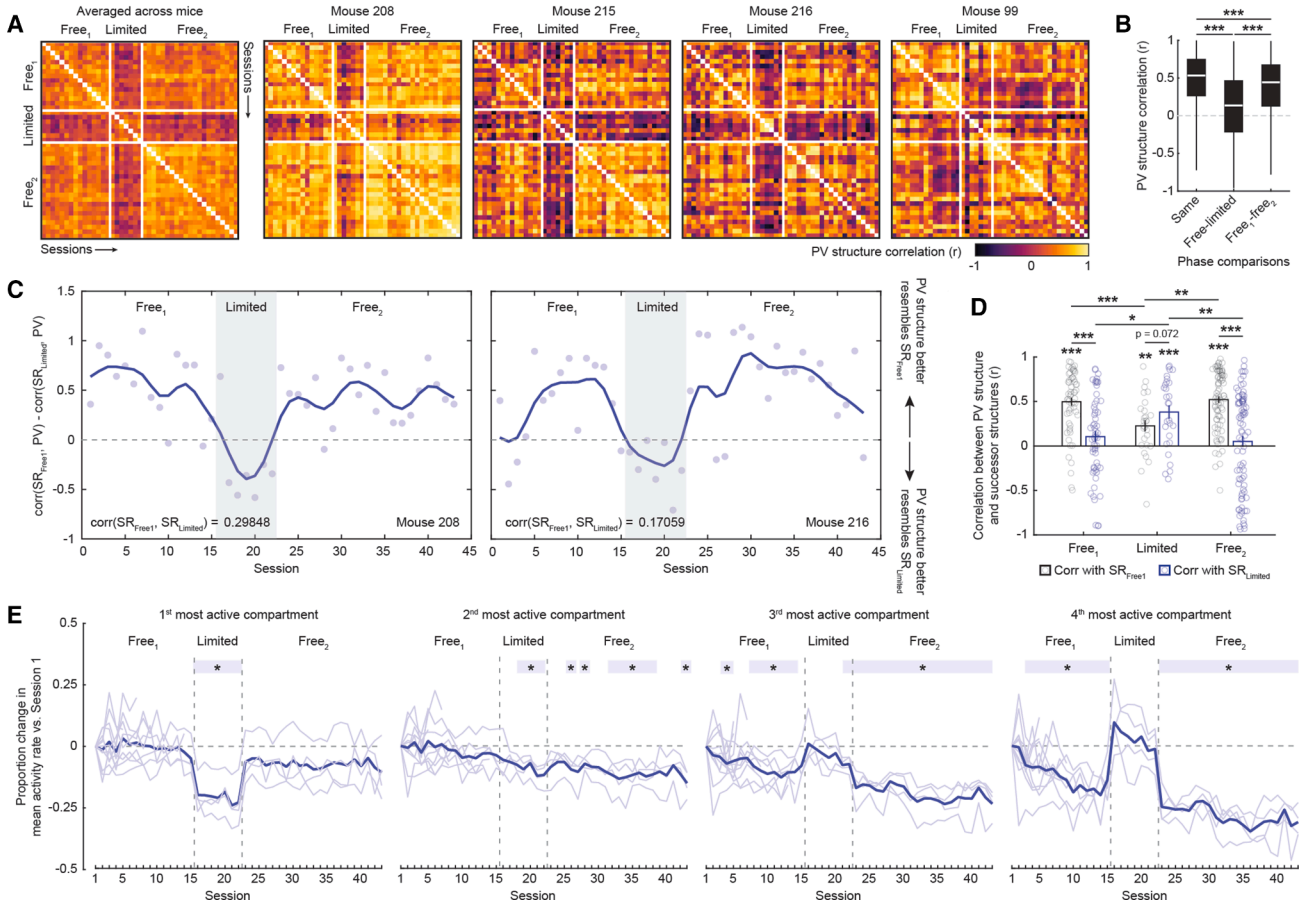

Figure 5. Limiting navigational options induces remapping that encodes the new predictive structure

(A) PV structure correlations across all 43 sessions, averaged across mice and separately for each mouse. White lines denote the boundaries of experimental phases.

(B) PV structure correlations for comparisons between sessions from the same phase, between Free and Limited phases, and between $Free_1$ and $Free_2$ phases.

(C) Difference in the correlation between PV structure and SR_{Free1} and $SR_{Limited}$ for two example mice. Dots indicate individual session values. Line depicts these data smoothed with a Gaussian kernel with 1.5 session standard deviation. Correlation between the SR structures is denoted in the lower right for each mouse.

(D) Correlations between PV structure and both SR_{Free1} and $SR_{Limited}$ for all sessions, aggregating across mice. For complete statistical information, see Table S1. Error bars denote SEM across sessions (dots).

(E) Change in mean activity rate versus the first session, as a function of most-active to least-active compartments. Soft lines are individual mice. Bold line is the mean across mice. Shaded box denotes sessions for which $p < 0.05$. Significance markers denote the outcome of an uncorrected t test versus zero for a given compartment and session. $^*p < 0.05$, $^{**}p < 0.01$, $^{***}p < 0.001$.

See also Figures S3–S5 and Tables S1 and S2.

(rank-sum tests: $Z(1891217) = 19.020$, $p = 1.163e{-}80$) or between $Free_1$ and $Free_2$ ($Z(926848) = -13.985$, $p = 1.917e{-}44$; Figure 5B). Correlations between $Free_1$ and $Free_2$ were numerically high but significantly weaker than same phase correlations ($Z(1874165) = 6.447$, $p = 1.143e{-}10$). This pattern of results indicates rapid remapping during the Limited manipulation, followed by a near return to the initial representational structure when this manipulation was relaxed.

Given that we observed rapid remapping during the limited phase, we next tested the key hypothesis that patterns of remapping during the limited phase would specifically resemble the new predictive structure. To do so, for each mouse, we computed the mean cumulative successor structure for both $free_1$ and limited navigation phases at the critical spatiotemporal scale determined above ($\gamma = 0.994$ and $\tau = -0.25$). We refer to these mean cumulative successor structures as SR_{Free1} and $SR_{Limited}$. These structures were only partially correlated with one another within each mouse ($r_{99} = 0.699$, $r_{208} = 0.299$, $r_{215} = -0.330$, and $r_{216} = 0.171$). We then correlated each of these successor structures with the PV structure for each session and compared these correlations across phases (Figures 5C and 5D). This analysis revealed that, during the $Free_1$ phase, PV structures were highly correlated with SR_{Free1} but uncorrelated with $SR_{Limited}$. Crucially, during the Limited phase, PV structures became correlated with $SR_{Limited}$, representing a significant increase over $Free_1$ phase correlations. Correlations with $SR_{Limited}$ numerically exceeded those with SR_{Free1}, though this difference was statistically marginal. Finally, during $Free_2$ the pattern of correlations reverted to that of $Free_1$. These results did not depend on the inclusion of pixels near the entryway in

Please cite this article in press as: Pecirno and Keinath, Environmental representations in mouse hippocampal CA1 reflect the predictive structure of navigation, Current Biology (2025), https://doi.org/10.1016/j.cub.2025.11.010

the analysis (Figure S3). Together, these results demonstrate that our manipulation specifically induced a pattern of remapping that matched the new predictive structure at the critical spatiotemporal scale, consistent with a predictive framework. We further note that the rapid reorganization of representational structure and apparent dissociable encoding of predictive structure during the Free and Limited phases suggests that other mechanisms, such as remapping of inputs,[61,62] also interact with the encoding of predictive structure in this paradigm.

Our findings indicate that limiting navigational options led to rapid encoding of new predictive structure, whereas the subsequent return to free navigation prompted a return of the $Free_1$ representational structure. This pattern suggests that the rate of encoding of predictive structure appears to be specific to the experimental phase. Though speculative, we asked whether we could observe other hallmarks of encoding that might corroborate this possibility. We noted that during $Free_1$ activity tended to become sparser over repeated sessions, as reflected by a decrease in the mean activity rate in dispreferred compartments (Figure 1F). This decrease roughly matched the optimal weighting of predictive structure across sessions ($\tau = -0.25$). We therefore characterized sparsity across the entire experiment utilizing our full dataset (Figure 5E). A linear mixed effects model of changes in activity rate with compartment, session number, and experimental phase as fixed factors and mouse ID as a random factor revealed multiple significant effects and interactions (significant main effects, session and phase; significant interactions, compartment by session, compartment by phase, and compartment by session by phase; Table S2). These reflect that, during Limited navigation, mean activity rates in dispreferred compartments returned to their initial levels but immediately reverted to their pre-limited rates during the subsequent $Free_2$. Qualitatively, mean activity rates in dispreferred compartments decreased across sessions during the Limited phase in a way echoing $Free_1$, while $Free_2$ resumed the trending decrease from $Free_1$. Mean activity rates in the most-active compartment also decreased during the Limited phase and returned to their $Free_1$ levels during the subsequent $Free_2$ phase. Overall, this pattern provides tentative evidence of phase-specific activity changes coinciding with enhanced encoding of predictive structure. Moreover, these findings suggest that the sparsity of the CA1 representation might serve as a proxy for the rate at which predictive structure is encoded.

A computational model encoding predictive structure over geometrically structured inputs can uniquely account for key results

We have shown that, in a multicompartment environment, CA1 instantiates idiosyncratic patterns of remapping between compartments, which are correlated with the similarity of predictive navigational structure on a particular spatiotemporal scale. To gain insight into how this pattern of results might arise, we implemented a series of computational models intended to mimic the input-output transformation carried out by CA1. We varied two aspects of these models: the spatial structure of their inputs and the transformation they compute on these inputs.

We considered inputs with two types of spatial structure. In both cases, inputs consisted of cells tuned to a single preferred location in each compartment. In the case of geometrically structured inputs, the preferred locations were in geometrically identical locations relative to the entryway in each compartment for a given cell (Figure 6A). In the case of randomly structured inputs, the preferred location randomly differed between each compartment for a given cell (Figure 6A). Contrasting the two will help us infer whether spatial tuning of inputs alone is sufficient to reproduce our results or whether geometric structure plays an important role.

We also considered three types of transformations. First, we considered a simple linear transformation (linear), where each CA1 cell received a small number of equally weighted inputs (STAR Methods). Second, we considered a predictive transformation (SR), where CA1 learns an approximation of the successor representation over its inputs, as explored previously.[26] In this case, the weight matrix M, which determines the strength of the connection from each input cell to each CA1 cell, is an online approximation of the successor representation, updated at each timestep according to

$$M \leftarrow M + \alpha[r(t) + \gamma Mr(t+1) - Mr(t)]\, r(t), \quad \text{(Equation 4)}$$

where $r(t)$ is the vector of input firing rates at time t, γ is the temporal discount factor, and α denotes the learning rate. The total input F_i to each CA1 cell i at each timestep t is then determined by

$$F_i = \sum_j M(i,j) r_j(t), \quad \text{(Equation 5)}$$

where M is the weight matrix at timestep t computed in Equation 4, and $r_j(t)$ is the firing rate of the j th input at timestep t. Third, we considered a version of the predictive transformation where a separate successor matrix M is learned for each compartment (multi-SR), and F_i for each CA1 cell is computed based on the M corresponding to the currently occupied compartment. Finally, for all transformations, the output of each CA1 cell was thresholded such that only the top 10% most-excited cells across the population were active during each timestep, with their activity normalized to a range between zero and one (STAR Methods).

To carry out our simulations, we used the actual navigational trajectories of our mice from the $Free_1$ phase of our experiment. For SR and multi-SR simulations, we used $\gamma = 0.994$, corresponding to the maximizing parameterization estimated above. To capture the decreasing weighting of cumulative experience over repeated sessions (i.e., $\tau = -0.25$), the learning rate α was set to decay exponentially at $\tau = -0.25$ from its initial value on session one (initial $\alpha = 0.005$).

For each combination of input structures and transformations, we first asked whether we observed reliable individual differences in representational structure, as we observed in our actual data. To this end, for each model, we correlated PV structures between all pairwise comparisons of sessions and contrasted comparisons from within the same mouse versus between different mice (Figure 6B). We found that all models with randomly structured inputs (which differed from mouse to mouse) recapitulated strong individual differences, as indicated by higher correlations for comparisons within a mouse than between different mice. On the other hand, geometrically structured inputs (which were identical across mice) did not

Please cite this article in press as: Pecirno and Keinath, Environmental representations in mouse hippocampal CA1 reflect the predictive structure of navigation, Current Biology (2025), https://doi.org/10.1016/j.cub.2025.11.010

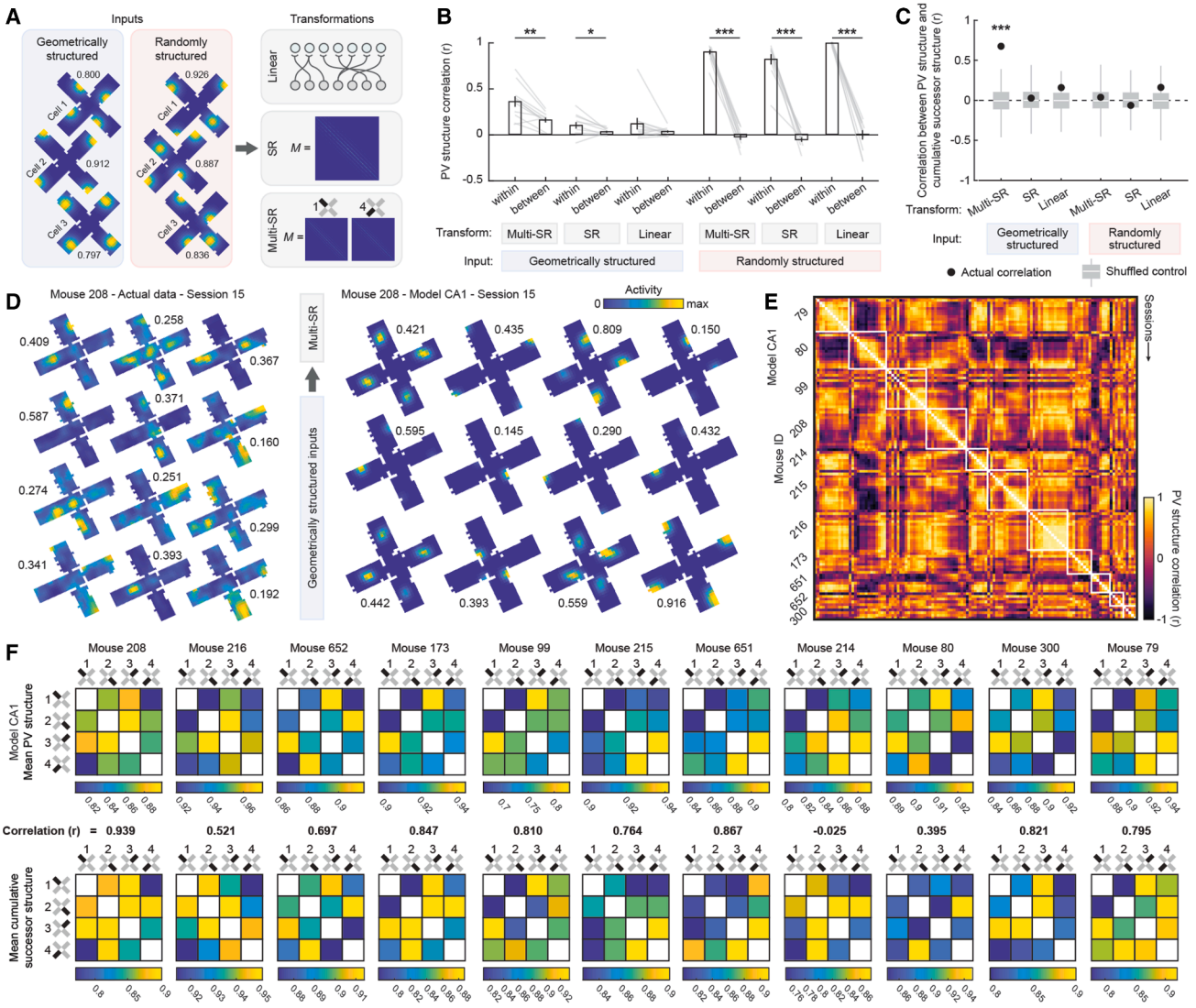

Figure 6. A predictive model with geometrically structured inputs replicates key results

(A) Schematic depicting possible model configurations. Peak activity rate noted for each rate map.

(B) PV structure correlations among sessions, separately for comparisons within the same mouse or between different mice, treating each mouse as the unit of analysis, and separately for each model (signed-rank tests; geo-multi-SR, $p = 2.930{-}03$; geo-SR, $p = 0.024$; geo-linear, $p = 0.101$; all random input models, $p = 9.766e{-}04$). Soft lines denote individual mice. Error bars denote SEM across mice.

(C) Correlations between the mean PV structure and the mean cumulative successor for each mouse, separately for each model. Black dots denote the true correlation. Gray box-and-whiskers denote the control distribution computed by shuffling cumulative successor structures across all sessions (1,000 shuffles, nonparametric p values estimated against surrogate distributions: geo-multi-SR, $p \sim 0.000$; geo-SR, $p = 0.430$; geo-linear, $p = 0.065$; rand-multi-SR, $p = 0.389$; rand-SR, $p = 0.690$; rand-linear, $p = 0.504$).

(D) Example rate maps for the same session from actual data and geo-multi-SR model CA1. Peak activity rate noted for each rate map.

(E) PV structure correlations across all pairwise comparisons of sessions for geo-multi-SR model CA1. White boxes bound session comparisons from the same mice.

(F) Mean PV structures for geo-multi-SR model CA1 and mean cumulative successor structures for all mice, with correlations noted, ordered as in Figure 3C.
*$p < 0.05$ **$p < 0.01$, ***$p < 0.001$.

See also Figure S6.

recapitulate individual differences in every case. Only when these inputs were coupled with learning of predictive structure (i.e., an SR or multi-SR transformation) were significant individual differences observed. These differences were particularly strong when predictive structure was learned separately for each compartment (i.e., multi-SR). These results demonstrate that individual differences are consistent with predictive encoding of geometrically structured inputs, although they may alternatively reflect other between-mouse differences, such as randomness in input structure.

Next, for each combination of inputs and transformations, we asked whether model PV structures were correlated with

cumulative successor structures, as we observed in our actual data. Computing cumulative successor structures at the maximizing parameters ($\gamma = 0.994$, $\tau = -0.25$), we found that PV structures were significantly correlated with cumulative successor structures in only one case (Figure 6C): when inputs were geometrically structured and predictive encoding was learned separately for each compartment (multi-SR). Neither factor was, on its own, sufficient, as other models including only one of these factors failed to produce significant correlations. Interestingly, environment-wide encoding of predictive structure (SR) failed to produce significant correlations, even when inputs were geometrically structured. This is because this model encodes only a single predictive structure for the entire environment, and the geometric repetition of inputs across compartments leads the model to learn the average predictive structure across all compartments rather than the predictive structure particular to each compartment.

In sum, among models tested, only a model with geometrically structured inputs and predictive encoding that is learned separately for each compartment can account for both individual differences in PV structure and the correlation between PV structure and successor structure that we observe in our actual data. For completeness, we provide additional visualizations of output from this model (Figures 6D–6F). Alternative models where geometrically structured inputs were embedded in a different orientational reference frame did not replicate these results (Figure S6), demonstrating that these outcomes also depend on other aspects of input features, even for geometrically structured inputs.

DISCUSSION

Here, we leveraged miniscope imaging of mouse CA1 in a multicompartment environment to test whether patterns of remapping exhibited hallmarks of predictive structure in a complex environment. We showed that different mice instantiated different patterns of remapping across identically shaped compartments in this paradigm. These patterns coincided with the similarity of predictive navigational structure on a seconds-long timescale, modestly overweighting early experience. Limiting navigational options in this environment induced a new pattern of remapping that specifically matched the new predictive navigational structure on this spatiotemporal scale. Finally, through computational modeling, we show that key results can be accounted for by a specific combination of predictive encoding operating over geometrically structured inputs learned separately within each compartment. Together, these results demonstrate that predictive navigational structure is one important determinant of hippocampal representational structure in complex environments, consistent with predictive theories of cognitive mapping.

In this experiment, we compared patterns of remapping across identical unrewarded compartments, from naiveté through extend experience, to isolate a potential influence of predictive navigational structure on the hippocampal representation distinct from confounding differences in world features, reward structure, or previous experience. Given that we find evidence of such a determinant under these conditions, we hypothesize that remapping across environments intentionally disambiguated by external cues[38,39,44,45] reflects both differences in input features and idiosyncratic navigational differences. Likewise, our results provide evidence that predictive structure is an ongoing determinant of CA1 representational structure, even in the absence of external rewards. Thus, we hypothesize that influences of reward structure on hippocampal coding[63–65] may reflect both differences in rewarding input features as well as differences in goal-directed navigational trajectories. Our findings also suggest that idiosyncratic predictive structure likely contributed to the results of other multicompartment paradigms,[41,48,53,54] even when individual differences in representational structure may have been masked by averaging across sessions and animals.

We relied on the successor representation as an operationalization of a predictive theory of hippocampal cognitive mapping.[21] In this model, the hippocampus can be understood as mapping temporally discounted transitions between states of the world, which can be defined not only by location but also by extra-spatial features. Indeed, one of the most compelling successes of this model is the ability to make quantitative predictions across scales (single cells, neural populations, and behavior), species (rodents and humans), and domains (physical, visual, and conceptual spaces).[21,66–68] Although we characterize transitions between locations as the state-defining feature in this work, we imagine that, in practice, the CA1 representational structure may be better understood as reflecting transitions among its spatially varying inputs, including those from CA3 and the entorhinal cortex.[26] Reflecting this, our modeling demonstrates that both the behavioral history of the navigator and the state-defining inputs play important roles in shaping representational structure in this paradigm, consistent with previous work.[26] Given these findings, we hypothesize that predictive structure also determines CA1 structure when navigating extra-spatial domains embedded in other input feature spaces. Additionally, we note that the successor representation is not the only theory consistent with a predictive determinant of CA1 representational structure.[22–24,69,70] Although our results are consistent with the predictions of this model, our experiment was not designed to adjudicate between competing theories of predictive cognitive mapping.

Our results demonstrate that CA1 representational structure most closely matches predictive structure when computed with a seconds-long temporal discount factor and overweighting early sessions. These characteristics are reminiscent of a unique form of hippocampal plasticity known as behavioral timescale synaptic plasticity (BTSP).[71,72] BTSP is a mechanism by which new place fields can be endogenously or artificially induced in previously silent CA1 cells by evoking a calcium-mediated plateau potential. Properties of induced place fields indicate that inputs active within a few seconds of this event are potentiated, that these fields exhibit skew that depends on the navigational trajectory during the initial plateau potential, and that endogenous plateau potentials are most common during initial experience.[71,73] It is thus possible that the predictive determinants of the CA1 representational structure we characterize here are a product of BTSP and, more generally, that BTSP provides a biological basis for the normative claims of predictive mapping theories. If so, then we would expect to observe an increase in plateau potentials not only in novel environments but

also during novel experiences that provoke representational change.[74] Our observations of changes in sparsity within and across experimental phases are roughly consistent with this. However, we interpret this finding with caution due to limitations inherent in our recording technique that do not allow us to distinguish plateau potentials from typical action potentials.

The critical spatiotemporal scale of predictive structure that we characterize here may also depend upon recording location within the hippocampus. It is known that the scale of spatial representations varies along the long dorsoventral axis of the hippocampus, progressing from finely tuned cells in the dorsal hippocampus to coarsely tuned cells in the ventral hippocampus.[75] Entorhinal inputs mirror this arrangement.[76–78] Even if the timescale of plasticity that encodes predictive structure were to be the same across this axis, differences in the scale of inputs might produce differences in the scale of encoded predictive structure.[79] In our work here, all populations were recorded from the dorsal hippocampus. Future work recording from the ventral hippocampus under similar conditions might address this possibility.

RESOURCE AVAILABILITY

Lead contact

Requests for further information and resources should be directed to, and will be fulfilled by, the lead contact, Dr. Alexandra T. Keinath (atk@uic.edu).

Materials availability

This study did not generate new, unique reagents.

Data and code availability

- All data generated by this study are publicly available through the Zenodo database [10.5281/zenodo.17438054].
- All code necessary to reproduce the analyses of this study is publicly available at https://github.com/akeinath/MouseCA1_PredictiveStructure_MulticompartmentEnvironment.
- Any additional information necessary to reproduce or reanalyze this study is available from the lead contact upon request.

ACKNOWLEDGMENTS

This work was supported by startup funding provided by the University of Illinois Chicago, as well as a UIC LAS CSSR seed grant. We would also like to thank J. Quinn Lee, Rachel Donka, and Rachel Barrett for feedback when drafting this manuscript and the reviewers for their thorough feedback throughout.

AUTHOR CONTRIBUTIONS

S.A.P. and A.T.K. contributed to experimental design, surgeries, recordings, analysis of data, and revising the manuscript. A.T.K. drafted the manuscript.

DECLARATION OF INTERESTS

The authors declare no competing interests.

STAR★METHODS

Detailed methods are provided in the online version of this paper and include the following:

SUPPLEMENTAL INFORMATION

Supplemental information can be found online at https://doi.org/10.1016/j.cub.2025.11.010.

Received: December 20, 2024
Revised: October 24, 2025
Accepted: November 5, 2025

REFERENCES

1. Tolman, E.C. (1948). Cognitive maps in rats and men. Psychol. Rev. *55*, 189–208. https://doi.org/10.1037/h0061626.
2. O'Keefe, J., and Nadel, L. (1978). The Hippocampus as a Cognitive Map (Oxford University Press).
3. McNaughton, B.L., Battaglia, F.P., Jensen, O., Moser, E.I., and Moser, M.-B. (2006). Path integration and the neural basis of the "cognitive map.". Nat. Rev. Neurosci. *7*, 663–678. https://doi.org/10.1038/nrn1932.
4. Peer, M., Brunec, I.K., Newcombe, N.S., and Epstein, R.A. (2021). Structuring knowledge with cognitive maps and cognitive graphs. Trends Cogn. Sci. *25*, 37–54. https://doi.org/10.1016/j.tics.2020.10.004.
5. Epstein, R.A., Patai, E.Z., Julian, J.B., and Spiers, H.J. (2017). The cognitive map in humans: spatial navigation and beyond. Nat. Neurosci. *20*, 1504–1513. https://doi.org/10.1038/nn.4656.
6. Poulter, S., Lee, S.A., Dachtler, J., Wills, T.J., and Lever, C. (2021). Vector trace cells in the subiculum of the hippocampal formation. Nat. Neurosci. *24*, 266–275. https://doi.org/10.1038/s41593-020-00761-w.
7. O'Keefe, J. (1976). Place units in the hippocampus of the freely moving rat. Exp. Neurol. *51*, 78–109. https://doi.org/10.1016/0014-4886(76)90055-8.
8. O'Keefe, J., and Burgess, N. (1996). Geometric determinants of the place fields of hippocampal neurons. Nature *381*, 425–428. https://doi.org/10.1038/381425a0.
9. Høydal, Ø.A., Skytøen, E.R., Andersson, S.O., Moser, M.-B., and Moser, E.I. (2019). Object-vector coding in the medial entorhinal cortex. Nature *568*, 400–404. https://doi.org/10.1038/s41586-019-1077-7.
10. Deshmukh, S.S., and Knierim, J.J. (2013). Influence of local objects on hippocampal representations: Landmark vectors and memory. Hippocampus *23*, 253–267. https://doi.org/10.1002/hipo.22101.
11. Knierim, J.J., Neunuebel, J.P., and Deshmukh, S.S. (2014). Functional correlates of the lateral and medial entorhinal cortex: objects, path integration and local–global reference frames. Philos. Trans. R. Soc. Lond. B Biol. Sci. *369*, 20130369. https://doi.org/10.1098/rstb.2013.0369.
12. Sargolini, F., Fyhn, M., Hafting, T., McNaughton, B.L., Witter, M.P., Moser, M.-B., and Moser, E.I. (2006). Conjunctive representation of position, direction, and velocity in entorhinal cortex. Science *312*, 758–762. https://doi.org/10.1126/science.1125572.
13. Hafting, T., Fyhn, M., Molden, S., Moser, M.-B., and Moser, E.I. (2005). Microstructure of a spatial map in the entorhinal cortex. Nature *436*, 801–806. https://doi.org/10.1038/nature03721.
14. Lever, C., Burton, S., Jeewajee, A., O'Keefe, J., and Burgess, N. (2009). Boundary vector cells in the subiculum of the hippocampal formation. J. Neurosci. *29*, 9771–9777. https://doi.org/10.1523/JNEUROSCI.1319-09.2009.

15. Ormond, J., and O'Keefe, J. (2022). Hippocampal place cells have goal-oriented vector fields during navigation. Nature *607*, 741–746. https://doi.org/10.1038/s41586-022-04913-9.

16. Barry, C., Lever, C., Hayman, R., Hartley, T., Burton, S., O'Keefe, J., Jeffery, K., and Burgess, N. (2006). The boundary vector cell model of place cell firing and spatial memory. Rev. Neurosci. *17*, 71–97. https://doi.org/10.1515/REVNEURO.2006.17.1-2.71.

17. Zhou, Y.-Q., Puliyadi, V., Chen, X., Lee, J.L., Zhang, L.-Y., and Knierim, J.J. (2024). Vector coding and place coding in hippocampus share a common directional signal. Nat. Commun. *15*, 10630. https://doi.org/10.1038/s41467-024-54935-2.

18. Taube, J.S., and Burton, H.L. (1995). Head direction cell activity monitored in a novel environment and during a cue conflict situation. J. Neurophysiol. *74*, 1953–1971. https://doi.org/10.1152/jn.1995.74.5.1953.

19. Taube, J.S. (1995). Head direction cells recorded in the anterior thalamic nuclei of freely moving rats. J. Neurosci. *15*, 70–86. https://doi.org/10.1523/JNEUROSCI.15-01-00070.1995.

20. Solstad, T., Boccara, C.N., Kropff, E., Moser, M.-B., and Moser, E.I. (2008). Representation of geometric borders in the entorhinal cortex. Science *322*, 1865–1868. https://doi.org/10.1126/science.1166466.

21. Stachenfeld, K.L., Botvinick, M.M., and Gershman, S.J. (2017). The hippocampus as a predictive map. Nat. Neurosci. *20*, 1643–1653. https://doi.org/10.1038/nn.4650.

22. George, D., Rikhye, R.V., Gothoskar, N., Guntupalli, J.S., Dedieu, A., and Lázaro-Gredilla, M. (2021). Clone-structured graph representations enable flexible learning and vicarious evaluation of cognitive maps. Nat. Commun. *12*, 2392. https://doi.org/10.1038/s41467-021-22559-5.

23. Whittington, J.C.R., Muller, T.H., Mark, S., Chen, G., Barry, C., Burgess, N., and Behrens, T.E.J. (2020). The Tolman-Eichenbaum machine: unifying space and relational memory through generalization in the hippocampal formation. Cell *183*, 1249–1263.e23. https://doi.org/10.1016/j.cell.2020.10.024.

24. Levenstein, D., Efremov, A., Eyono, R.H., Peyrache, A., and Richards, B. (2024). Sequential predictive learning is a unifying theory for hippocampal representation and replay. Preprint at bioRxiv. https://doi.org/10.1101/2024.04.28.591528.

25. Chandra, S., Sharma, S., Chaudhuri, R., and Fiete, I. (2025). Episodic and associative memory from spatial scaffolds in the hippocampus. Nature *638*, 739–751. https://doi.org/10.1038/s41586-024-08392-y.

26. de Cothi, W., and Barry, C. (2020). Neurobiological successor features for spatial navigation. Hippocampus *30*, 1347–1355. https://doi.org/10.1002/hipo.23246.

27. Bennett, L., de Cothi, W., Muessig, L., Rodrigues, F.R., Cacucci, F., Wills, T.J., Sun, Y., Giocomo, L.M., Lever, C., Poulter, S., et al. (2025). Unifying subicular function: a predictive map approach. Preprint at bioRxiv. https://doi.org/10.1101/2024.11.06.622306.

28. Derdikman, D., Whitlock, J.R., Tsao, A., Fyhn, M., Hafting, T., Moser, M.-B., and Moser, E.I. (2009). Fragmentation of grid cell maps in a multicompartment environment. Nat. Neurosci. *12*, 1325–1332. https://doi.org/10.1038/nn.2396.

29. Keinath, A.T., Epstein, R.A., and Balasubramanian, V. (2018). Environmental deformations dynamically shift the grid cell spatial metric. eLife *7*, e38169. https://doi.org/10.7554/eLife.38169.

30. Moore, J.J., Cushman, J.D., Acharya, L., Popeney, B., and Mehta, M.R. (2021). Linking hippocampal multiplexed tuning, Hebbian plasticity and navigation. Nature *599*, 442–448. https://doi.org/10.1038/s41586-021-03989-z.

31. Zutshi, I., Apostolelli, A., Yang, W., Zheng, Z.S., Dohi, T., Balzani, E., Williams, A.H., Savin, C., and Buzsáki, G. (2025). Hippocampal neuronal activity is aligned with action plans. Nature *639*, 153–161. https://doi.org/10.1038/s41586-024-08397-7.

32. Nieh, E.H., Schottdorf, M., Freeman, N.W., Low, R.J., Lewallen, S., Koay, S.A., Pinto, L., Gauthier, J.L., Brody, C.D., and Tank, D.W. (2021). Geometry of abstract learned knowledge in the hippocampus. Nature *595*, 80–84. https://doi.org/10.1038/s41586-021-03652-7.

33. Climer, J.R., Davoudi, H., Oh, J.Y., and Dombeck, D.A. (2025). Hippocampal representations drift in stable multisensory environments. Nature *645*, 457–465. https://doi.org/10.1038/s41586-025-09245-y.

34. Hardcastle, K., Maheswaranathan, N., Ganguli, S., and Giocomo, L.M. (2017). A multiplexed, heterogeneous, and adaptive code for navigation in medial entorhinal cortex. Neuron *94*, 375–387.e7. https://doi.org/10.1016/j.neuron.2017.03.025.

35. Liberti, W.A., Schmid, T.A., Forli, A., Snyder, M., and Yartsev, M.M. (2022). A stable hippocampal code in freely flying bats. Nature *604*, 98–103. https://doi.org/10.1038/s41586-022-04560-0.

36. Wiener, S.I., Paul, C.A., and Eichenbaum, H. (1989). Spatial and behavioral correlates of hippocampal neuronal activity. J. Neurosci. *9*, 2737–2763. https://doi.org/10.1523/JNEUROSCI.09-08-02737.1989.

37. Sun, C., Yang, W., Martin, J., and Tonegawa, S. (2020). Hippocampal neurons represent events as transferable units of experience. Nat. Neurosci. *23*, 651–663. https://doi.org/10.1038/s41593-020-0614-x.

38. Leutgeb, S., Leutgeb, J.K., Barnes, C.A., Moser, E.I., McNaughton, B.L., and Moser, M.-B. (2005). Independent codes for spatial and episodic memory in hippocampal neuronal ensembles. Science *309*, 619–623. https://doi.org/10.1126/science.1114037.

39. Bostock, E., Muller, R.U., and Kubie, J.L. (1991). Experience-dependent modifications of hippocampal place cell firing. Hippocampus *1*, 193–205. https://doi.org/10.1002/hipo.450010207.

40. Jeffery, K.J., and Anderson, M.I. (2003). Dissociation of the geometric and contextual influences on place cells. Hippocampus *13*, 868–872. https://doi.org/10.1002/hipo.10162.

41. Fuhs, M.C., Vanrhoads, S.R., Casale, A.E., McNaughton, B., and Touretzky, D.S. (2005). Influence of path integration versus environmental orientation on place cell remapping between visually identical environments. J. Neurophysiol. *94*, 2603–2616. https://doi.org/10.1152/jn.00132.2005.

42. Tanni, S., de Cothi, W., and Barry, C. (2022). State transitions in the statistically stable place cell population correspond to rate of perceptual change. Curr. Biol. *32*, 3505–3514.e7. https://doi.org/10.1016/j.cub.2022.06.046.

43. Lever, C., Wills, T., Cacucci, F., Burgess, N., and O'Keefe, J. (2002). Long-term plasticity in hippocampal place-cell representation of environmental geometry. Nature *416*, 90–94. https://doi.org/10.1038/416090a.

44. Colgin, L.L., Leutgeb, S., Jezek, K., Leutgeb, J.K., Moser, E.I., McNaughton, B.L., and Moser, M.-B. (2010). Attractor-map versus autoassociation based attractor dynamics in the hippocampal network. J. Neurophysiol. *104*, 35–50. https://doi.org/10.1152/jn.00202.2010.

45. Wills, T.J., Lever, C., Cacucci, F., Burgess, N., and O'Keefe, J. (2005). Attractor dynamics in the hippocampal representation of the local environment. Science *308*, 873–876. https://doi.org/10.1126/science.1108905.

46. Plitt, M.H., and Giocomo, L.M. (2021). Experience-dependent contextual codes in the hippocampus. Nat. Neurosci. *24*, 705–714. https://doi.org/10.1038/s41593-021-00816-6.

47. Nilchian, P., Wilson, M.A., and Sanders, H. (2022). Animal-to-animal variability in partial hippocampal remapping in repeated environments. J. Neurosci. *42*, 5268–5280. https://doi.org/10.1523/JNEUROSCI.3221-20.2022.

48. Duvelle, É., Grieves, R.M., Liu, A., Jedidi-Ayoub, S., Holeniewska, J., Harris, A., Nyberg, N., Donnarumma, F., Lefort, J.M., Jeffery, K.J., et al. (2021). Hippocampal place cells encode global location but not connectivity in a complex space. Curr. Biol. *31*, 1221–1233.e9. https://doi.org/10.1016/j.cub.2021.01.005.

49. Pnevmatikakis, E.A., and Giovannucci, A. (2017). NoRMCorre: An online algorithm for piecewise rigid motion correction of calcium imaging data. J. Neurosci. Methods *291*, 83–94. https://doi.org/10.1016/j.jneumeth.2017.07.031.

50. Pnevmatikakis, E.A., Soudry, D., Gao, Y., Machado, T.A., Merel, J., Pfau, D., Reardon, T., Mu, Y., Lacefield, C., Yang, W., et al. (2016). Simultaneous denoising, deconvolution, and demixing of calcium imaging data. Neuron *89*, 285–299. https://doi.org/10.1016/j.neuron.2015.11.037.

51. Zhou, P., Resendez, S.L., Rodriguez-Romaguera, J., Jimenez, J.C., Neufeld, S.Q., Giovannucci, A., Friedrich, J., Pnevmatikakis, E.A., Stuber, G.D., Hen, R., et al. (2018). Efficient and accurate extraction of in vivo calcium signals from microendoscopic video data. eLife *7*, e28728. https://doi.org/10.7554/eLife.28728.

52. Friedrich, J., Zhou, P., and Paninski, L. (2017). Fast online deconvolution of calcium imaging data. PLoS Comput. Biol. *13*, e1005423. https://doi.org/10.1371/journal.pcbi.1005423.

53. Spiers, H.J., Hayman, R.M.A., Jovalekic, A., Marozzi, E., and Jeffery, K.J. (2015). Place field repetition and purely local remapping in a multicompartment environment. Cereb. Cortex *25*, 10–25. https://doi.org/10.1093/cercor/bht198.

54. Grieves, R.M., Jenkins, B.W., Harland, B.C., Wood, E.R., and Dudchenko, P.A. (2016). Place field repetition and spatial learning in a multicompartment environment. Hippocampus *26*, 118–134. https://doi.org/10.1002/hipo.22496.

55. Karlsson, M.P., and Frank, L.M. (2008). Network dynamics underlying the formation of sparse, informative representations in the hippocampus. J. Neurosci. *28*, 14271–14281. https://doi.org/10.1523/JNEUROSCI.4261-08.2008.

56. Fenton, A.A. (2024). Remapping revisited: how the hippocampus represents different spaces. Nat. Rev. Neurosci. *25*, 428–448. https://doi.org/10.1038/s41583-024-00817-x.

57. Anderson, M.I., and Jeffery, K.J. (2003). Heterogeneous modulation of place cell firing by changes in context. J. Neurosci. *23*, 8827–8835. https://doi.org/10.1523/JNEUROSCI.23-26-08827.2003.

58. Krishnan, S., Heer, C., Cherian, C., and Sheffield, M.E.J. (2022). Reward expectation extinction restructures and degrades CA1 spatial maps through loss of a dopaminergic reward proximity signal. Nat. Commun. *13*, 6662. https://doi.org/10.1038/s41467-022-34465-5.

59. Sosa, M., Plitt, M.H., and Giocomo, L.M. (2025). A flexible hippocampal population code for experience relative to reward. Nat. Neurosci. *28*, 1497–1509. https://doi.org/10.1038/s41593-025-01985-4.

60. Pettit, N.L., Yuan, X.C., and Harvey, C.D. (2022). Hippocampal place codes are gated by behavioral engagement. Nat. Neurosci. *25*, 561–566. https://doi.org/10.1038/s41593-022-01050-4.

61. Lykken, C.M., Kanter, B.R., Nagelhus, A., Carpenter, J., Guardamagna, M., Moser, E.I., and Moser, M.-B. (2025). Functional independence of entorhinal grid cell modules enables remapping in hippocampal place cells. Preprint at bioRxiv. https://doi.org/10.1101/2025.09.24.677985.

62. Fyhn, M., Hafting, T., Treves, A., Moser, M.-B., and Moser, E.I. (2007). Hippocampal remapping and grid realignment in entorhinal cortex. Nature *446*, 190–194. https://doi.org/10.1038/nature05601.

63. Jarzebowski, P., Hay, Y.A., Grewe, B.F., and Paulsen, O. (2022). Different encoding of reward location in dorsal and intermediate hippocampus. Curr. Biol. *32*, 834–841.e5. https://doi.org/10.1016/j.cub.2021.12.024.

64. Sato, M., Mizuta, K., Islam, T., Kawano, M., Sekine, Y., Takekawa, T., Gomez-Dominguez, D., Schmidt, A., Wolf, F., Kim, K., et al. (2020). Distinct mechanisms of over-representation of landmarks and rewards in the hippocampus. Cell Rep. *32*, 107864. https://doi.org/10.1016/j.celrep.2020.107864.

65. Gauthier, J.L., and Tank, D.W. (2018). A dedicated population for reward coding in the hippocampus. Neuron *99*, 179–193.e7. https://doi.org/10.1016/j.neuron.2018.06.008.

66. Momennejad, I., Russek, E.M., Cheong, J.H., Botvinick, M.M., Daw, N.D., and Gershman, S.J. (2017). The successor representation in human reinforcement learning. Nat. Hum. Behav. *1*, 680–692. https://doi.org/10.1038/s41562-017-0180-8.

67. de Cothi, W., Nyberg, N., Griesbauer, E.-M., Ghanamé, C., Zisch, F., Lefort, J.M., Fletcher, L., Newton, C., Renaudineau, S., Bendor, D., et al. (2022). Predictive maps in rats and humans for spatial navigation. Curr. Biol. *32*, 3676–3689.e5. https://doi.org/10.1016/j.cub.2022.06.090.

68. Garvert, M.M., Saanum, T., Schulz, E., Schuck, N.W., and Doeller, C.F. (2023). Hippocampal spatio-predictive cognitive maps adaptively guide reward generalization. Nat. Neurosci. *26*, 615–626. https://doi.org/10.1038/s41593-023-01283-x.

69. Savelli, F., and Knierim, J.J. (2019). Origin and role of path integration in the cognitive representations of the hippocampus: computational insights into open questions. J. Exp. Biol. *222*, jeb188912. https://doi.org/10.1242/jeb.188912.

70. Zutshi, I., Apostolelli, A., Yang, W., Zheng, Z. (Sam), Dohi, T., Balzani, E., Williams, A.H., Savin, C., and Buzsáki, G. (2024). Hippocampal neuronal activity is aligned with action plans. Preprint at bioRxiv. https://doi.org/10.1101/2024.09.05.611533.

71. Bittner, K.C., Milstein, A.D., Grienberger, C., Romani, S., and Magee, J.C. (2017). Behavioral time scale synaptic plasticity underlies CA1 place fields. Science *357*, 1033–1036. https://doi.org/10.1126/science.aan3846.

72. Milstein, A.D., Li, Y., Bittner, K.C., Grienberger, C., Soltesz, I., Magee, J.C., and Romani, S. (2021). Bidirectional synaptic plasticity rapidly modifies hippocampal representations. eLife *10*, e73046. https://doi.org/10.7554/eLife.73046.

73. Madar, A.D., Dong, C., and Sheffield, M.E.J. (2023). BTSP, not STDP, drives shifts in hippocampal representations during familiarization. Preprint at bioRxiv. https://doi.org/10.1101/2023.10.17.562791.

74. Monaco, J.D., Rao, G., Roth, E.D., and Knierim, J.J. (2014). Attentive scanning behavior drives one-trial potentiation of hippocampal place fields. Nat. Neurosci. *17*, 725–731. https://doi.org/10.1038/nn.3687.

75. Kjelstrup, K.B., Solstad, T., Brun, V.H., Hafting, T., Leutgeb, S., Witter, M.P., Moser, E.I., and Moser, M.-B. (2008). Finite scale of spatial representation in the hippocampus. Science *321*, 140–143. https://doi.org/10.1126/science.1157086.

76. Brun, V.H., Solstad, T., Kjelstrup, K.B., Fyhn, M., Witter, M.P., Moser, E.I., and Moser, M.B. (2008). Progressive increase in grid scale from dorsal to ventral medial entorhinal cortex. Hippocampus *18*, 1200–1212. https://doi.org/10.1002/hipo.20504.

77. Stensola, H., Stensola, T., Solstad, T., Frøland, K., Moser, M.-B., and Moser, E.I. (2012). The entorhinal grid map is discretized. Nature *492*, 72–78. https://doi.org/10.1038/nature11649.

78. Giocomo, L.M., Stensola, T., Bonnevie, T., Van Cauter, T., Moser, M.-B., and Moser, E.I. (2014). Topography of head direction cells in medial entorhinal cortex. Curr. Biol. *24*, 252–262. https://doi.org/10.1016/j.cub.2013.12.002.

79. Momennejad, I., and Howard, M.W. (2018). Predicting the future with multi-scale successor representations. Preprint at bioRxiv. https://doi.org/10.1101/449470.

80. Mathis, A., Mamidanna, P., Cury, K.M., Abe, T., Murthy, V.N., Mathis, M.W., and Bethge, M. (2018). DeepLabCut: markerless pose estimation of user-defined body parts with deep learning. Nat. Neurosci. *21*, 1281–1289. https://doi.org/10.1038/s41593-018-0209-y.

81. Skaggs, W.E., McNaughton, B.L., and Gothard, K.M. (1993). An information-theoretic approach to deciphering the hippocampal code. Adv. Neural Inf. Process. Syst. 1030–1037.

82. McKenzie, S., Huszár, R., English, D.F., Kim, K., Christensen, F., Yoon, E., and Buzsáki, G. (2021). Preexisting hippocampal network dynamics constrain optogenetically induced place fields. Neuron *109*, 1040–1054.e7. https://doi.org/10.1016/j.neuron.2021.01.011.

Please cite this article in press as: Pecirno and Keinath, Environmental representations in mouse hippocampal CA1 reflect the predictive structure of navigation, Current Biology (2025), https://doi.org/10.1016/j.cub.2025.11.010

STAR★METHODS

KEY RESOURCES TABLE

REAGENT or RESOURCE	SOURCE	IDENTIFIER
Bacterial and virus strains		
AAV9.syn.GCaMP8f.WPRE	addGene	Cat#162376-AAV9
Deposited data		
Imaging data	Generated by this study	10.5281/zenodo.17438054
Experimental models: Organisms/strains		
Mouse: C57BL/6	The Jackson Laboratory	RRID: IMSR_JAX:000664
Software and algorithms		
Custom MATLAB code	Generated by this study	https://github.com/akeinath/MouseCA1_PredictiveStructure_MulticompartmentEnvironment

EXPERIMENTAL MODEL AND STUDY PARTICIPANT DETAILS

Eleven naive mice (C57BL/6, The Jackson Laboratory; 6 male, 5 female) were housed in pairs in 20 cm x 40 cm cages which included running wheels and additional enrichment. Mice were kept on a 14-hour light/10-hour dark cycle at 23°C and 30% humidity with food and water ad libitum. All experiments were carried out during the light portion of the light/dark cycle, and in accordance with University of Illinois Chicago Animal Use and Care Committee (protocol #23008) and with AAALAC guidelines.

METHOD DETAILS

Surgeries

During all surgeries, mice were anesthetized via inhalation of a combination of oxygen and 5% isoflurane before being transferred to the stereotaxic frame (David Kopf Instruments), where anesthesia was maintained via inhalation of oxygen and 0.5%–2.5% isoflurane for the duration of the surgery. Body temperature was maintained with a heating pad and eyes were hydrated with gel (Optixcare). Meloxicam (2 mg kg^{-1}) and saline (0.5 ml) were administered subcutaneously at the beginning of each surgery. Preparation for recordings involved three surgeries per mouse.

First, at the age of six to ten weeks, each mouse was transfected with a 400 nl injection of the calcium reporter GCaMP8f via the viral construct AAV9.syn.GCaMP8f.WPRE with an original titer of 2.3 x 10^{13} GC ml^{-1} (Addgene) diluted at a 1 part virus to 7 parts sterile artificial cerebrospinal fluid before surgical microinjection. While expression in both principal cells and inhibitory populations is possible under the syn promoter, it is likely that the large majority of cells we record are excitatory given their sparse transients.

Three weeks post-injection, a 1.8mm diameter gradient refractive index (GRIN) lens (Edmund Optics) was implanted above dorsal CA1 (Referenced to bregma: ML = 2.0 mm, AP = -2.1 mm; Referenced to brain surface: DV = -1.35 mm). Implantation required aspiration of intervening cortical tissue. In addition to the GRIN lens, two stainless steel screws were threaded into the skull above the contralateral hippocampus and prefrontal cortex to stabilize the implant. Dental cement (C&B Metabond) was applied to secure the GRIN lens and anchor screws to the skull. A silicone adhesive (Kwik-Sil, World Precision Instruments) was applied to protect the top surface of the GRIN lens until the next surgery.

Three weeks after lens implantation, an aluminum baseplate was affixed via dental cement (C&B Metabond) to the skull of the mouse, which would later secure the miniaturized fluorescent endoscope (miniscope) in place during recording. The miniscope/baseplate was mounted to a stereotaxic arm for lowering above the implanted GRIN lens until the field of view contained visible cell segments and dental cement was applied to affix the baseplate to the skull. A polyoxymethylene cap was affixed to the baseplate when the mice were not being recorded to protect the baseplate and lens.

After surgery, animals were continuously monitored until they recovered. For the initial two days after surgery mice were provided with additional doses of meloxicam for pain management. One week following baseplating, to familiarize mice with the recording procedure and to monitor the quality of cell activity, we recorded mice daily in a 75 cm x 75 cm square open field for 10 min to 30 min per day. When recording quality was deemed of sufficiently high quality based on a stable number of cells across days, rapid transients, and a high proportion of cells with stable place fields within day (>50% of cells versus shuffled controls), mice began the multicompartment experiment. Mice typically met these criteria 2+ weeks following baseplating.

Please cite this article in press as: Pecirno and Keinath, Environmental representations in mouse hippocampal CA1 reflect the predictive structure of navigation, Current Biology (2025), https://doi.org/10.1016/j.cub.2025.11.010

Apparatus

The recording environment was constructed of white Lego base and white acrylic walls (Professional Plastics). All walls had a height of 20 cm. All compartments were 20 cm x 35 cm, with a 20cm central chamber. No other internal directional cues were provided, but the apparatus was closer to one external grey room wall which could serve as an external directional cue. During recording, the environment was dimly lit by an LED lamp positioned to reduce shadows, and a white-noise machine was used to mask any uncontrolled sounds. All sessions were 30 or 40 min (depending on signal strength to minimize photobleaching), and only one session was recorded per day. On rare occasions (~2%) sessions were impacted by equipment failures, and sessions were terminated early; data from these sessions were not analyzed. During all free exploration sessions, mice were placed in the center of the environment at the start of the session facing the nearer external grey room wall. During limited navigation sessions, mice were placed in the first room at the start of the session also facing the nearer external grey wall. Mice were not intentionally disoriented prior to recording, and the stability of patterns of remapping across days suggests that they remained oriented throughout. The recording environment was cleaned between recordings with veterinarian-grade disinfectant.

Data acquisition

In vivo calcium videos were recorded with a UCLA miniscope (v3; miniscope.org) containing a monochrome CMOS imaging sensor (MT9V032C12STM, ON Semiconductor) connected to a custom data acquisition (DAQ) box (miniscope.org) with a lightweight, flexible coaxial cable. The DAQ was connected to a PC with a USB 3.0 SuperSpeed cable and controlled with Miniscope custom acquisition software (miniscope.org; software version v4). The outgoing excitation LED was set to between 5%–30%, depending on the mouse to maximize signal quality with the minimum possible excitation light to mitigate the risk of photobleaching. Gain was adjusted to match the dynamic range of the recorded video to the fluctuations of the calcium signal for each recording to avoid saturation. Behavioral video data were recorded by a webcam mounted above the environment. The DAQ simultaneously acquired behavioral and cellular imaging streams at 30 Hz as FFV1 losslessly-compressed AVI files and all recorded frames were timestamped for post-hoc alignment.

QUANTIFICATION AND STATISTICAL ANALYSIS

Data preprocessing

Calcium imaging data were preprocessed prior to analyses via a pipeline of open source MATLAB (MathWorks; version R2024a) functions to correct for motion artifacts,[49] segment cells and extract transients.[50] The motion-corrected calcium imaging data were manually inspected to ensure that motion correction was effective and did not introduce additional artifacts. Following this preprocessing pipeline, the spatial footprints of all cells were manually verified to remove lens artifacts. Finally, to estimate the spike trains which gave rise to the transients we recorded, we implemented a second-order autoregressive deconvolution algorithm.[52] This nonnegative vector was then binarized such that any frame with a nonzero likelihood was treated as active (i.e. 1), otherwise it was treated as not active (i.e. 0). All further analysis was conducted on this binary activity vector.

Position data were inferred from behavioral videos via DeepLabCut[80] tracking the nose, ears, and tail base of the mouse. The average between the two ears was taken as the position of the mouse in all analyses. Periods where estimates of either ear positions were low-confidence (<0.90) or the estimated distance between the ears was unrealistic were excluded and position was linearly interpolated across these timepoints (<0.5% of timepoints). Position data were then resampled via linear interpolation based on system clock timestamping to estimate the position at each time when imaging frames were collected.

Data analysis

All analyses were conducted using the binarized nonnegative spike train estimates inferred via a second-order autoregressive deconvolution, henceforth the *activity* vector.

Rate maps

Rate maps for each cell were computed by dividing the environment (or each compartment) into 2.5 cm x 2.5 cm pixels, computing the mean activity rate at each pixel for that cell, and then smoothing the result map with an isotropic gaussian kernel with standard deviation of 2.5 cm. These maps were then corrected for edge artifacts and artifacts induced by smoothing over unsampled pixels as follows (MATLAB function *nanconv* available at https://www.mathworks.com/matlabcentral/fileexchange/41961-nanconv). First, a second map where sampled pixels are set to one and all other pixels are set to zero was computed. This map was then smoothed with the same kernel, and each rate map was divided by this smoothed map. Unsampled pixels (pixels that were not sampled on any frame) were excluded from further comparisons.

Split-half stability

To characterize the stability of each cell's spatial tuning during a session, we computed its split-half stability by computing whole environment rate maps using only the first half or second half of the data from that session and correlating the two rate maps. To determine the statistical significance of these correlations, we compared this true correlation to a surrogate distribution computed by randomly circularly shifting the position vector relative to the activity vector by at least 30 seconds and recomputing the resulting correlation 1000 times. Cells with true correlations exceeding the 95% of this surrogate distribution were considered spatially-stable and included in further analysis.

Please cite this article in press as: Pecirno and Keinath, Environmental representations in mouse hippocampal CA1 reflect the predictive structure of navigation, Current Biology (2025), https://doi.org/10.1016/j.cub.2025.11.010

Spatial information content

To characterize the specificity of each cell's spatial tuning during a session, we computed its spatial information content from its whole environment rate map as described previously[81] via the equation:

$$\text{Spatial information content} = \sum_i \mathbf{p}_i \mathbf{a}_i \log\left(\frac{\mathbf{a}_i}{\overline{\mathbf{a}}}\right) \quad \text{(Equation 6)}$$

where i is the rate map pixel index, $\mathbf{p}_i$ is the probability of sampling pixel i, $\mathbf{a}_i$ is the mean firing rate at pixel i , and $\overline{\mathbf{a}}$ is the mean firing rate across all pixels. To determine the statistical significance of these values, we compared the true spatial information content to a surrogate distribution computed by randomly circularly shifting the position vector relative to the activity vector by at least 30 seconds and recomputing the resulting correlation 1000 times. Cells with true correlations exceeding the 95% of this surrogate distribution were considered spatially tuned and included in further analysis.

Similarity structures

Population vector correlations between compartments were computed by aligning these rate maps by the entryway, and reshaping rate maps to be one pixel long, concatenating these linearized rate maps for all cells from each compartment, and computing the correlation between these vectors. This measure takes into account both changes in the spatial distributions of firing and relative changes in firing rate. Mean activity rate correlations between compartments were computed by correlating the vector of mean activity rates for all included cells between compartments. Successor structure and cumulative successor structure were computed as described in the main text. To compute successor matrices, position data were binned to 5 cm x 5 cm pixels, and the timestep was set to 1/30th of a second to match the frame rate of data acquisition.

Local versus global orientation analyses

In supplemental analyses, we contrast rate map correlations and population vector correlations between compartments when aligning compartments by their entryway (*local orientation*, as in previous analyses) versus by a common 'north' (*global orientation*). To make global orientation comparisons possible, all rate maps were rescaled after smoothing into squares using MATLAB's *imresize* to be 14 x 14 pixels prior to computing these correlations.

Computational modeling

To compute activity vectors of model inputs, first each compartment was divided into a grid of possible preferred locations at 1.25 cm x 1.25 cm increments; each cell was assigned one of these preferred locations, with the grid of preferred locations chosen to yield a sizable population of 448 input cells total. For geometrically structured inputs, each cell had the same preferred location across all compartments, aligned by their entryways. For randomly structured inputs, the assignment of preferred locations was randomly shuffled across cells for each compartment. Once assigned, each cell kept its preferred locations for all sessions. At each timestep, the activity of each cell was determined from its distance to its nearest preferred location according to a gaussian distribution with standard deviation 5 cm. Finally, input activity vectors were normalized to scale from [0, 1] inclusive. Each transformation received identical input traces for the geometrically structured inputs and randomly structured inputs.

For the linear transformation, each CA1 cell received a random number of inputs on the range [2, 16] drawn from a Poisson distribution with $\lambda = 4$. These inputs were chosen from the input population at random and given equal weight (i.e. 1). All other inputs were assigned a weight of 0 for that CA1 cell. Once assigned, these weights were constant across all sessions. SR and multi-SR transformations are described in the main text. In all cases, the successor matrices were initialized as the identity matrix.

Finally in all cases the output O_i from CA1 cell i was determined at each timestep by

$$O_i = \frac{\Theta(F_i - T_{90\%})}{\max_j\left(\Theta(F_j - T_{90\%})\right)} \quad \text{(Equation 7)}$$

where F_i is the total input to CA1 cell i, $T_{90\%}$ is a dynamic threshold corresponding to the F of the cell with the 90th percentile F across the population at that timestep, and

$$\Theta(x) = \begin{cases} x \text{ if } x > 0 \\ 0 \text{ otherwise} \end{cases} \quad \text{(Equation 8)}$$

The result of this thresholding and normalization is that only 10% of CA1 cells are active during each timestep with output rates ranging from [0, 1]. This dynamic normalization is intended to mimic competition among principal cells in CA1,[82] and is especially useful when changes in connectivity during learning lead to large changes in excitatory drive as is often the case in our SR and multi-SR simulations. For each model, we simulated 448 CA1 cells, matching the number of input cells. Output vectors were treated like the activity vectors of our actual data in all further analyses. SR and multi-SR transformations were deterministic and therefore a single iteration is presented in the main text. A single iteration of the linear transformation model was also included to match the presentation of SR and multi-SR simulations, despite some additional randomness in its implementation. However, we note that we have run approximately 10 iterations at the identical parameterization and in all cases the results closely resemble those presented in the main text. Modeled activity vectors were treated the same as our binarized calcium trace activity vectors in all further analyses.

In the supplement, we include simulations where the geometrically structured inputs are oriented according to a global reference frame (i.e. a 'common north') across compartments (Figure S6). To do so, first each compartment was divided into a grid of possible

Please cite this article in press as: Pecirno and Keinath, Environmental representations in mouse hippocampal CA1 reflect the predictive structure of navigation, Current Biology (2025), https://doi.org/10.1016/j.cub.2025.11.010

preferred locations at 5% increments scaled to the size of each axis, so that each compartment had 20 x 20 possible preferred locations. For globally-oriented geometrically structured inputs, each cell had the same preferred location across all compartments (in percentile of each axis length), aligned by global north (see Figure S6 for examples). For randomly structured inputs, the assignment of preferred locations was randomly shuffled across cells for each compartment. Once assigned, each cell kept its preferred locations for all sessions. At each timestep, the activity of each cell was determined from its distance to its nearest preferred location according to a gaussian distribution with standard deviation 5 cm. Finally, input activity vectors were normalized to scale from [0, 1] inclusive. Each transformation received identical input traces for the geometrically structured inputs and randomly structured inputs. All other aspects of supplemental models matched the main text models described above.

Histological validation of expression and recording targets

After experiments, animals were perfused to verify GRIN lens placement. Mice were deeply anesthetized and intracardially perfused with 4% paraformaldehyde in PBS. Brains were dissected and post-fixed with the same fixative. Coronal sections (50 μm) of the entire hippocampus were cut using a vibratome and sections were mounted directly on glass slides. Sections were split and half of all sections were stained for DAPI and mounted with Fluoromount-G (Southern Biotechnology) to localize GRIN lens placement and to evaluate viral expression. Due to the large imageable surface but restricted miniscope field of view ($\sim$0.5 mm x $\sim$0.8 mm), we were unable to determine more specific localization of populations within the hippocampus for mice recorded with 1.8 mm lenses.

Statistics and reproducibility

All statistical tests are noted where the corresponding results are reported throughout the main text and supplement. All tests were conducted in MATLAB (MathWorks; version R2024a). All tests were uncorrected 2-tailed tests unless otherwise noted. Z-values for nonparametric rank-sum and signed-rank tests were not estimated or reported for comparisons with fewer than 15 datapoints. Box plots portray the minimum and maximum (whiskers), upper and lower quartiles (boxes), and median (cinch/bolded line). All correlations are Pearson's correlations unless otherwise noted.